Volume 23
Number 6
14 February 2021
Pages 3681–4040

PCCP

Physical Chemistry Chemical Physics

rsc.li/pccp

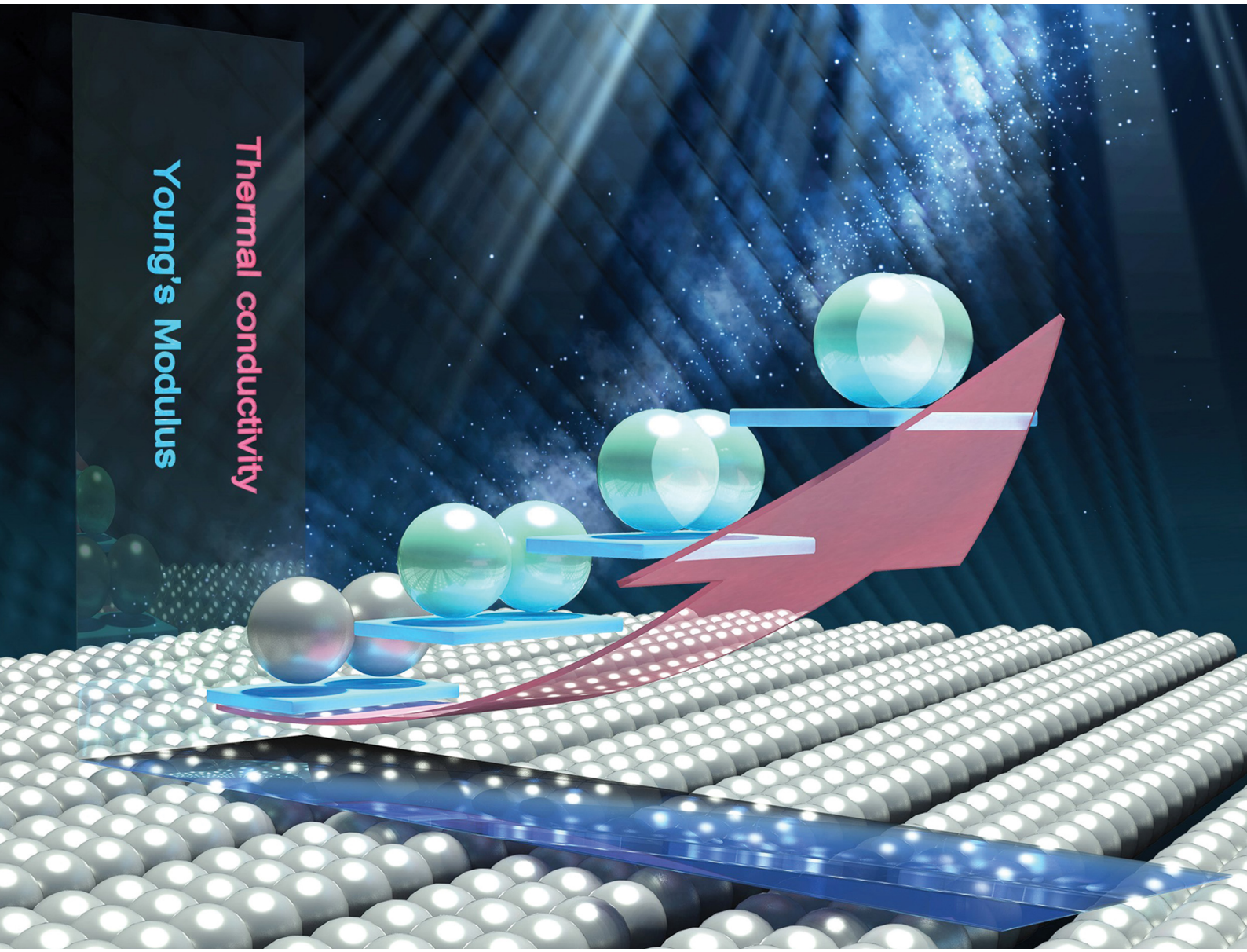

ISSN 1463-9076

ROYAL SOCIETY OF CHEMISTRY

PAPER

George Fytas *et al.*

Surface contacts strongly influence the elasticity and thermal conductivity of silica nanoparticle fibers

PCCP

ROYAL SOCIETY OF CHEMISTRY

PAPER

View Article Online
View Journal | View Issue

Cite this: *Phys. Chem. Chem. Phys.*, 2021, **23**, 3707

Surface contacts strongly influence the elasticity and thermal conductivity of silica nanoparticle fibers†

Yu Cang,[ab] Bohai Liu,‡[c] Sudatta Das,‡[b] Xiangfan Xu,[c] Jingli Xie,[d] Xu Deng[d] and George Fytas*[b]

Granular materials are often encountered in science and engineering disciplines, in which controlling the particle contacts is one of the critical issues for the design, engineering, and utilization of their desired properties. The achievable rapid fabrication of nanoparticles with tunable physical and chemical properties facilitates tailoring the macroscopic properties of particle assemblies through contacts at the nanoscale. Models have been developed to predict the mechanical properties of macroscopic granular materials; however, their predicted power in the case of nanoparticle assemblies is still uncertain. Here, we investigate the influence of nanocontacts on the elasticity and thermal conductivity of a granular fiber comprised of close-packed silica nanoparticles. A complete elastic moduli characterization was realized by non-contact and non-destructive Brillouin light spectroscopy, which also allowed resolving the stiffness of the constituent particles *in situ*. In the framework of effective medium models, the strong enhancement of the elastic moduli is attributed to the formation of adhesive nanocontacts with physical and/or chemical bondings. The nanoparticle contacts are also responsible for the increase in the fiber thermal conductivity that emphasizes the role of interface thermal resistance, which tends to be ignored in most porosity models. This insight into the fundamental understanding of structure–property relationships advances knowledge on the manipulation of granular systems at the nanoscale.

Received 13th October 2020,
Accepted 30th November 2020

DOI: 10.1039/d0cp05377e

rsc.li/pccp

Introduction

In the last three decades, much research effort has focused on the synthesis of metallic and non-metallic nanoparticles (NPs) with controlled chemistry, size, shape, and composition driven by their intriguing quantized behavior like that of atoms.[1] This enormous progress has boosted new research on the assembly of these NPs into hierarchical-architectured materials. Their unanticipated novel properties and consequently a plethora of applications have stimulated further research efforts in this large field of nanomaterials.[2–4] More recently, free-standing assemblies have been fabricated to eliminate unwanted interactions with solder substrates leading to radiation damage or kinetically trapped non-equilibrium structures. Nanoparticle assemblies can find numerous applications in acoustic, optoelectronics, and thermoelectric devices.[2,4–6] For the realization of these technological applications, an understanding of the phononic properties is of equal importance. The propagation of phonons not only yields the elasticity, which is important for stability, but also allows the characterization of the interparticle contacts, which enhance heat conduction and the rigidity of colloid-based structures. Coherent phonons can be either injected by an optical pump pulse in picosecond acoustic techniques[5,7] or probed by spontaneous Brillouin light spectroscopy (BLS).[8–10] The latter is a non-destructive technique that can resolve both propagated phonons with the wave vector and polarization resolution and localized phonons associated with the colloid elastic vibrations.[11–13] The concurrent access to effective medium phonons and particle vibrations enables independent monitoring of the film and the constituent component elasticity.

Among different colloidal NP assembly shapes, uniform macroscale colloidal fibers have been reported with wide application perspectives, such as the fabrication of microchannels[14] and photonic devices,[15] due to the excellent controllability of their morphology and periodicity. Recently, harnessing crack engineering, a unique strategy was developed to fabricate transparent centimeter-scale fibers without a template.[16] The fiber

[a] *School of Aerospace Engineering and Applied Mechanics, Tongji University, 100 Zhangwu Road, 200092, Shanghai, China*
[b] *Max Planck Institute for Polymer Research, Ackermannweg 10, 55128, Mainz, Germany. E-mail: fytas@mpip-mainz.mpg.de*
[c] *Center for Phononics and Thermal Energy Science, School of Physical Science and Engineering, Tongji University, Shanghai, 200092, China*
[d] *Institute of Fundamental and Frontier Sciences, University of Electronic Science and Technology of China, Chengdu, 610054, China*

† Electronic supplementary information (ESI) available. See DOI: 10.1039/d0cp05377e

‡ B. L. and S. D. are equally contributed to this work.

dimensions could be controlled simply by tuning the physical parameters, such as solvent composition, suspension descending rate, and NP volume fraction, and its large-scale production has shown great promise in practical applications. For instance, the fibers can be utilized as a platform of Ag-coated nanostructured surfaces exhibiting considerably higher sensitivity for probing small molecules compared to a typical smooth silicon wafer in the surface-enhanced Raman scattering detection. To realize broad applications, exploring the fundamental properties and understanding their relationships with the structure is an important requisite. It was found that the mechanical stiffness of NP-assembled fibers could be reinforced by thermal annealing without significantly altering the nanostructure; however, the physics behind these strong enhancements was not discussed.[16] Also other properties, such as thermal conductivity, which is important in practical applications, have not been examined either.

In this work, we address these questions by investigating the complete elasticities and thermal conductivity of free-standing fibers comprised of SiO_2 NPs for different annealing durations combined with complementary continuum mechanical and heat transport analysis. To achieve this, we performed non-contact elastic characterizations on silica fibers and their constituent particles *via* Brillouin light spectroscopy (BLS). The experimental data were interpreted by effective medium models, thus enabling an assessment of the roles of the nanocontacts and the adhesion processes in different annealing times. Moreover, we measured the thermal conductivity of the silica fibers using a T-bridge method, in which the increase with annealing time was well represented by a contact radius-controlled heat conduction path.

Results and discussion

Preparation of the silica fibers

The silica (SiO_2) fibers were prepared from the controlled crack formation, as illustrated in Fig. 1a–c.[16] Here, as the solvent (water/ethanol) of SiO_2 NPs (diameter $d = 95 \pm 7$ nm) colloidal suspension evaporates between 323 and 363 K (Fig. 1a), their self-assembly into a wet colloidal film on the vial's wall (substrate) is driven by the capillary and Marangoni flows (Fig. 1b). Meanwhile, cracks are formed in the wet film and propagate vertically downwards. A centimeter-scale fiber consisting of self-assembled NPs is formed between two adjacent cracks as the evaporation process is completed, as shown in Fig. 1c. The shape of the pristine (without annealing) silica fibers and its nanostructure of the surface were determined here by optical (Fig. 1d) and scanning electron microscopy (SEM) (Fig. 1e). In order to further improve the mechanical stiffness, the pristine fibers were placed under thermal treatment at $T = 1173$ K for different annealing times (0.5, 2, and 4 h). The corresponding SEM images shown in Fig. 1f and Fig. S1 (ESI†) indicate that the nanostructures after annealing were almost identical to the pristine state. The samples coded as F-annealing time are listed in Table 1 along with structural and physical parameters of the fibers and the constituent NPs.

Complete elasticity of the silica fibers and their constituent nanoparticles

For a transparent sample, BLS measures the sound velocities of both longitudinal (LA) and transverse (TA) acoustic phonons at hypersonic frequency (GHz), and hence can uniquely determine the complete material elasticities if the sample density is known. The sound velocity of the LA phonon is detectable in a polarized (VV) BLS spectrum, where VV denotes vertical polarization of both the incident ($\mathbf{k_i}$) and scattered ($\mathbf{k_s}$) lights relative to the scattering plane ($\mathbf{k_i}$,$\mathbf{k_s}$). Fig. 2a exemplifies the VV BLS spectra (anti-Stokes side, grey lines) of the pristine and three annealed silica fibers recorded in the transmission scattering geometry at a phonon wavevector $q = 0.0167$ nm^{-1} and $T = 294$ K. At the transmission scattering geometry illustrated in Fig. S2 and Section 1.2 in ESI,† the phonon wavevector $\mathbf{q}$ is parallel to the film plane and its magnitude $q_{\parallel} = \left(\frac{4\pi}{\lambda}\right)\sin(\alpha)$, with $\lambda = 532$ nm being

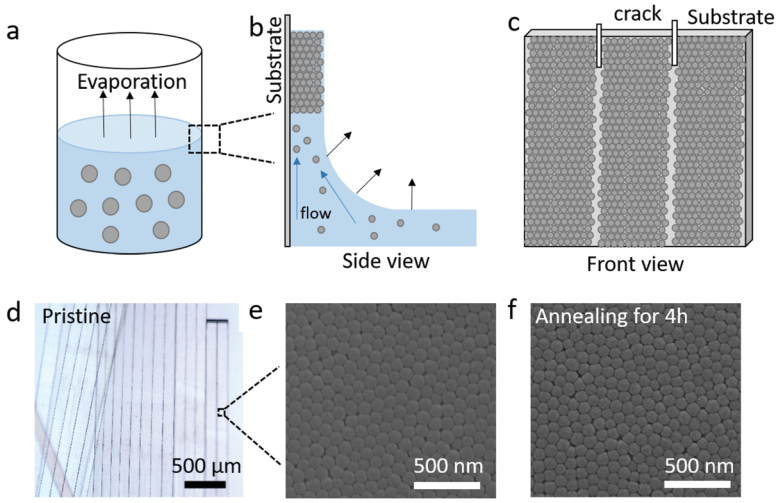

Fig. 1 (a–c) Scheme of the fiber preparation. (a) Evaporation of a suspension of silica nanoparticles in ethanol/water. (b) Self-assembly of SiO_2 NPs on the vial wall driven by the capillary and Marangoni flows. (c) Directed and uniform development of cracks accompanying the drying of the solvent. (d and e) Optical and SEM images of pristine fibers. (f) SEM image of the annealed fiber, treated at $T = 1173$ K for 4 h.

Table 1 Properties of the fibers and their constituent SiO_2 nanoparticles

Sample code	Annealing duration[a] (hour)	Density of fibers, ρ (kg m^{-3})	Core–core distance, d_c (nm)	Diameter of SiO_2 NPs, d (nm)	Porosity[b], p (%)	Refractive index, n	Density of SiO_2 NPs[c], ρ_{NP} (kg m^{-3})	Adhesion energy[d], W (J m^{-2})
F-0	0	1273 ± 107	89 ± 10	95 ± 7	0.33	1.32	1900	0.14
F-05	0.5	1602 ± 119	85 ± 7	90 ± 4	0.26	1.34	2200	0.39
F-2	2	1639 ± 77	80 ± 8	90 ± 4	0.24	1.33	2200	1.42
F-4	4	1683 ± 156	77 ± 6	90 ± 4	0.22	1.34	2200	3.17

[a] Annealing at T = 1173 K. [b] Porosity $p = \rho/\rho_{NP}$. [c] Estimated from the density-dependent modulus in Fig. 3. [d] W is calculated eqn (3) assuming A = 16.

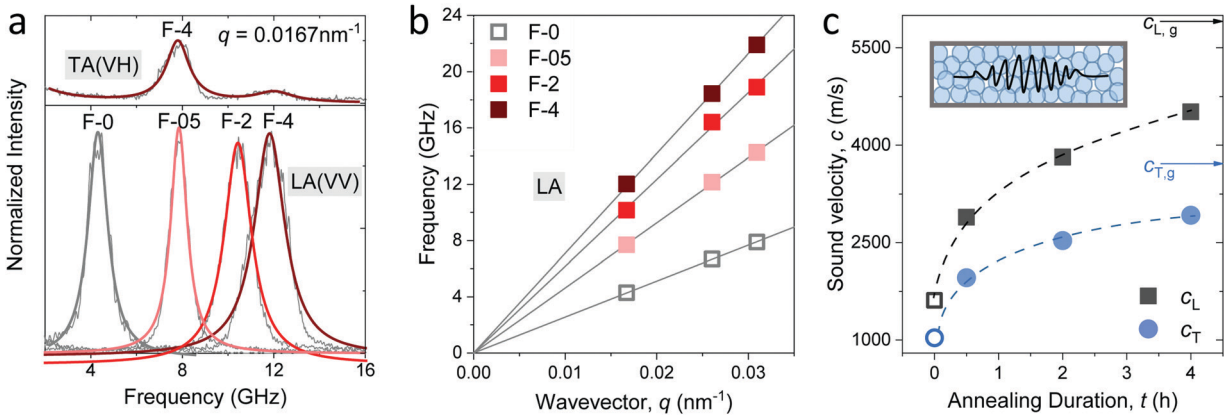

Fig. 2 (a) Normalized polarized (VV) Brillouin light scattering (BLS) spectra at a scattering wave vector q = 0.0167 nm^{-1} assigned to the longitudinal acoustic (LA) phonon in the indicated silica fibers. Top panel: The normalized depolarized (VH) spectrum at q = 0.0167 nm^{-1} assigned to the transverse acoustic (TA) phonon in F-4. (b) The linear dispersion relation, frequency *vs.* wave vector q, for the LA phonon obtained from the VV BLS spectra recorded at in-plane and out-of-plane q's for the four fibers. (c) Longitudinal, c_L, and transverse, c_T, sound velocities in the four silica fibers. The corresponding values in amorphous glass are indicated by the black and blue arrows respectively. Inset: Schematic of GHz phonon propagation in the fibers. All the open symbols refer to the pristine F-0 without annealing. The solid lines are linear fits of $f(q)$ with zero intercept whereas the dashed lines are guided to the eye.

the wavelength of the incident light, which is independent of the materials' refractive index; *i.e.*, q = 0.0167 nm^{-1} for an incident angle $\alpha = 45°$. The VV BLS spectra for all fibers in Fig. 2a are well represented by single Lorentzian lineshapes (red lines) yielding the frequencies f of LA phonons at q = 0.0167 nm^{-1}. The linear acoustic dispersions $f(q)$ of LA phonons are shown in Fig. 2b, where q's (> 0.024 nm^{-1}) directed normal to the film plane were achieved in the reflection and backscattering geometries (Fig. S2 and Section 1.2 in ESI†), respectively. The magnitude of this out-of-plane $q_\perp = \frac{4\pi}{\lambda}\sqrt{n^2 - \cos^2\alpha}$ now depends on the fiber refractive index, n. Assuming elastic isotropy, $f = cq/2\pi$ is linear throughout q's range yielding $n = 1.33 \pm 0.02$ which is, within error, the same for all the samples. The corresponding longitudinal sound velocity $c_L (= 2\pi f/q)$ for different annealing durations is shown in Fig. 2c (black squares).

Access to the sound velocity of transverse acoustic (TA) phonon, c_T, is necessary to calculate the shear and hence Young's modulus. This is feasible if the depolarized (VH) BLS spectra are sufficiently strong to be recorded; VH denotes the vertical and parallel polarizations of the incident and scattered lights relative to the $(\mathbf{k_i},\mathbf{k_s})$ plane, respectively. The top panel in Fig. 2a displays the VH spectrum (grey line) of F-4 at q = 0.0167 nm^{-1} along with its representation (red line) by two Lorentzians. The low-frequency strong peak was assigned to the TA phonon, whereas the weaker peak at a higher frequency is the LA phonon in the VV spectrum due to the scrambling of the scattered light polarization. The transverse sound velocity $c_T (= 2\pi f/q)$ in the four fibers is shown in Fig. 2c (blue circles).

The sound velocities shown in Fig. 2c represent the effective medium values in the fibers consisting of randomly close-packed SiO_2 NPs. Both c_L and c_T increased abruptly by about 85% from the pristine (F-0, open symbols) to the fiber annealed for a short time (F-05) and a reduced increase to about 50% with prolonged annealing to 4 h (F-4). Note that even for the longest annealed F-4 sample, both c_L and c_T remained ~22% less than the corresponding values of typical amorphous glass (arrows in Fig. 2c). An increase in the effective medium sound velocities can, in principle, arise from denser packing (decreasing porosity), densification of the SiO_2 NPs, and/or due to the increasing adhesion forces between NPs. The increase in the fiber density by 25% from F-0 to F-05 and only by 5% from F-05 to F-4 was clearly lower than the corresponding increase in the sound velocities, suggesting that packing alone cannot account for the higher sound velocities (hardening) of the fibers upon annealing. Prior to the discussion of the elastic moduli of the fibers and understanding the origin of its elastic enhancements, knowledge

of the elastic properties of the constituent silica NPs is a prerequisite. Experimental access to the elasticity of NPs and their assembled structure simultaneously by BLS is, for the first time, reported in the granular materials.[5,7,17,18]

It is well established that NPs exhibit vibrations, in analogy to the electron motion in atoms. For non-interacting spheres, the resolved lowest-frequency mode by BLS can be assigned to the quadrupole (1,2) vibration, where 1 and 2 denote the radial and angular momentum, respectively.[13,19] This is a resonance localized mode and hence $f(1,2)$ is q-independent. For isolated NPs, the (1,2) mode should be a single symmetric peak at $f(1,2) = A(\nu_{NP})\ c_{T,NP}/d$, where $c_{T,NP}$ denotes the transverse sound velocity of the NP with diameter d and A is a dimensionless constant depending on the NP's Poisson's ratio, ν_{NP}.[19] Here, $f(1,2)$ is much higher than the frequencies of the LA and TA phonons at the probed q's of BLS (Fig. 2c). Fig. 3a shows this high-frequency (1,2) mode in the VV BLS spectra (grey lines) of F-0 and F-4 recorded at the backscattering geometry. Due to the d^{-1} dependence, the size polydispersity leads to a broadening of the (1,2) peaks.[20] The (1,2) mode of both F-0 and F-4 was not single and hence is represented (blue lines) by two Lorentzian lines (red lines) centered at the frequencies f_1 and $f_2(>f_1)$. The splitting of the (1,2) mode, resulting from interactions between two NPs,[13,21] suggests the presence of surface contacts and adhesion between SiO_2 NPs, which was much more pronounced for F-4. The effect of interaction can be accounted for by computing $f(1,2) = 2f_1 - f_2$ which is utilized to compute $c_{T,NP}$ $(= f(1,2)d/A)$ using $A = 0.84$.[22,23]

The computed transverse sound velocities of the SiO_2 NPs, $c_{T,NP}$, shown in the lower panel of Fig. 3b strongly increased (by 65%) with annealing from 0 to 0.5 h, but became virtually constant with prolonged annealing. For the pristine SiO_2 NPs in F-0, $c_{T,NP} = 2310 \pm 50$ m s^{-1} was slightly lower than the $c_{T,NP} = 2390$ m s^{-1} of the NPs with $\rho = 1960$ kg m^{-3}.[23] Since $c_{T,NP}$ mainly depends on the NPs' density, we assigned $\rho = 1900$ kg m^{-3} to the pristine SiO_2 NPs in F-0 based on the density-dependence of the modulus;[23] whereby this density value is in good agreement with the literature values of Stöber silica NPs.[24] For the SiO_2 NPs in the three annealed fibers, the virtually constant $c_{T,NP} = 3720 \pm 50$ m s^{-1} reached the $c_{T,bulk} = 3740$ m s^{-1} of bulk fused silica with the density $\rho = 2200$ kg m^{-3}.[23,25] The fiber density was found to display a similar behavior with annealing as depicted in the inset in the lower panel of Fig. 3b. Building on this data consistency, the upper panel of Fig. 3b depicts the variation of the normalized transverse sound velocity in the silica fiber, $c_T/c_{T,NP}$, with the particle volume fraction $(1 - p)$. Interestingly, this ratio was not constant but a stronger increase was observed with the annealing duration, indicating a strengthening of the cohesive forces between SiO_2 NPs, as will be discussed for the elasticity moduli next.

Access to both c_T and c_L in the silica fibers allows an estimation of their complete effective elastic moduli, including Young's (E), shear (G), and bulk (K) moduli. The $G = \rho c_T^2$, $E = 2G(1 + \nu)$ and Poisson's ratio $\nu = \dfrac{a-2}{2a-2}$ with $a = \dfrac{c_L^2}{c_T^2}$ are shown in Fig. 4a. The trend of the fiber elasticities (E and G) with annealing was clearly distinct from the G_{NP} of the constituent SiO_2 NPs (Fig. 3b); whereby the former significantly increased with annealing time, whereas the latter was virtually constant.

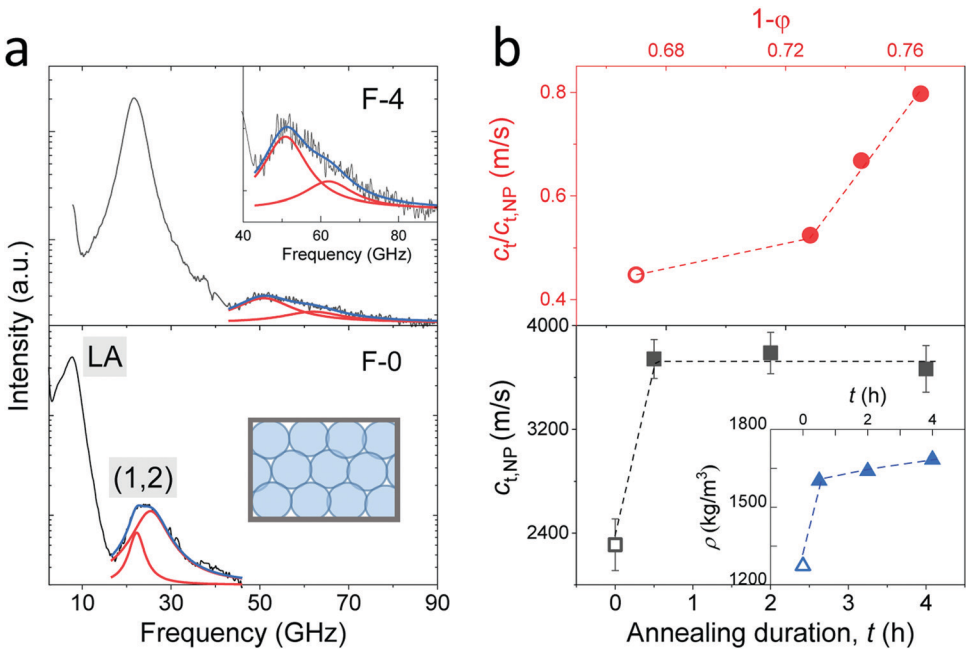

Fig. 3 (a) Polarized BLS spectra of the F-0 (low panel) and F-4 (upper panel) fibers recorded at the backscattering geometry. The resolved modes are assigned to LA phonon for the fibers and quadrupole mode (1,2) for the SiO_2 NPs as indicated in the plot. The (1,2) mode is represented (blue lines) by a double Lorentzian (red lines) shapes. A zoom-in of the vibration spectrum in F-4 is shown in the inset to the upper panel. (b) Low panel: The transverse sound velocity of SiO_2 NPs ($c_{T,NP}$) *vs.* annealing duration, t, where the density of the fibers (Table 1) is presented in the inset. Upper panel: Normalized transverse sound velocity of the fibers, $c_T/c_{T,NP}$, as a function of NP volume fraction, $1 - p$, with p being the porosity (Table 1). For the pristine fibers, the physical quantities are denoted by empty symbols in (b).

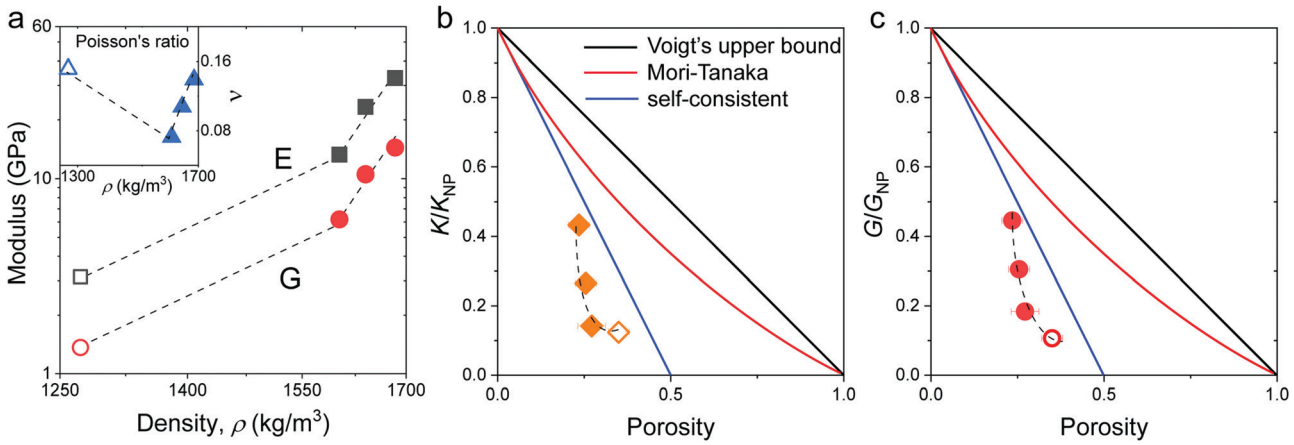

Fig. 4 (a) Young's (E, black squares) and shear (G, red circles) moduli as a function of density for the four silica fibers. Inset: Poisson's ratio ν *vs.* fiber density. Normalized to that of the constituent SiO_2 particles, K/K_{NP} in (b) and G/G_{NP} in (c), plotted as a function of the porosity. The color lines denote different model predictions: Voigt's upper bound (black), Mori-Tanaka (red), and self-consistent (green) models (Section 2.1 in ESI†). The dashed lines are guided to the eye. All open symbols refer to the pristine F-0.

Hence additional effects should become important for the observed enhanced elasticity of the fibers in the annealing regime (0.5–4 h). For the Poisson's ratio of fiber ν, it dropped from 0.16 (F-0) to 0.08 in F-05 and then increased toward the bulk value (ν = 0.17) with prolonging the annealing time.

Surface contacts

To shed light on the origin of the elasticity enhancement, we employed different continuum mechanics models for the interpretation of the experimental moduli of the silica fibers. First, we utilized the representative elementary volume (REV) models proposed for porous materials with a random packing of NPs (Section 2.1 in ESI†). The simple linear mixing rule for the effective Young's modulus, $E = (1 - p)E_{NP}$, (Voigt's upper bound) assumes a similar deformation of holes and NPs. Two additional approaches, Mori–Tanaka's[26] and self-consistent approximation,[27] take into account the shape and percolation of pores, yielding reliable predictions for some porous structures.[28] However, all these REV models cannot quantitatively represent the experimental data shown in Fig. 4b and c, whereby the normalized moduli K/K_{NP} and G/G_{NP} of the fibers increase much stronger with porosity than the theoretical prediction made by different REV models. It should be noted that all REV models envisage the NPs as a homogenous matrix and ignore mutual interactions. The latter, however, have been found to play a decisive role in the effective properties, especially in the close packing structures as shown next.

In the framework of effective medium theory, the effective elastic moduli of disordered granular systems with identical particles of diameter d can be related to the normal (k_n) and tangential (k_s) contact stiffness between NPs.[29,30] Accordingly, k_n and k_s are given by

$$k_n = \left(c_L^2 - \frac{4}{3}c_T^2\right)\frac{6\pi d\rho_{NP}}{Z} \quad (1a)$$

$$k_s = \left(c_T^2 - \frac{1}{3}c_L^2\right)\frac{12\pi d\rho_{NP}}{Z} \quad (1b)$$

where $Z = 2 + 11(1 - \varphi)^2$ is the mean coordinate number depending on the packing density.[31] For random close packing with a porosity of ~35%, the literature value of Z falls in the range of 6–9.[31] The computed k_n and k_s (eqn (1)) for the four silica fibers are presented in Fig. 5a. Both k_n and k_s (see scheme in the inset to Fig. 5a) determined by the K (= $M - 4G/3$) and G moduli displayed a similar density dependence with the silica fiber elastic moduli in Fig. 4a. The ratio $\frac{k_n}{k_s} = \frac{1+\nu}{1-4\nu}$ (eqn (1)) is controlled by the fiber Poisson's ratio ν (Fig. 4a) and varied in the range of 1.5–3 (top panel of Fig. 5b). Note, the SiO_2 NP's contact interactions impact the experimental sound velocities but are not explicitly presented in eqn (1).

Several microstructural continuum models have quantitatively addressed the relation of the contact stiffness to the micro-deformation at the interface.[29,32,33] Digby proposed a phenomenological description[29] of k_n and k_s for smooth particles with the contact radius r_a, and an initially bonded area of radius r_b (see scheme in the inset to Fig. 5b) as a function of the constituent NP elasticity:

$$k_n = \frac{4G_{NP}r_a}{1 - \nu_{NP}} \quad (2a)$$

$$k_s = \frac{8G_{NP}r_b}{2 - \nu_{NP}} \quad (2b)$$

where G_{NP} and ν_{NP} are the shear modulus (Fig. 3b) and Poisson's ratio (= 0.17) of the constituent NPs, respectively. Note that the application of eqn (2) requires independent information on G_{NP}, which in our case was obtained from the NP vibration frequency (Fig. 3). The two radii ratio is related to the ratio k_n/k_s and ν_{NP}. When an applied force is imposed on the particles, r_a is assumed to increase, whereas r_b is rather robust. The different responses of r_b and r_a to loading leads to a decoupling of k_n and k_s in eqn (2). The Digby model has adequately described sintered systems, such as poly(methyl methacrylate) NPs,[34] but failed to describe systems like titanium dioxide NPs.[18]

Since cohesive forces can be introduced in the annealing process, we utilized the Digby model for a rationalization of the

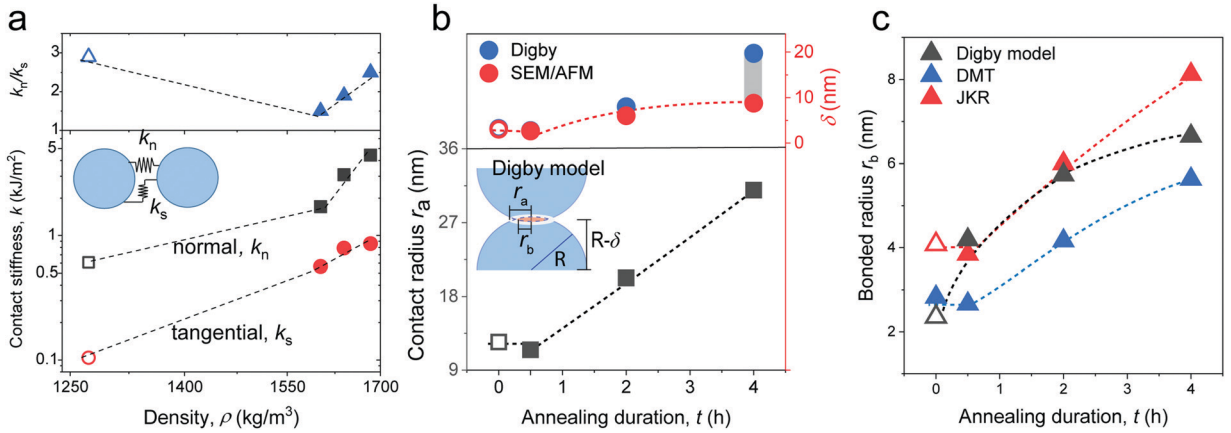

Fig. 5 (a) Normal (k_n) (black squares) and tangential (k_s) (red circles) stiffness computed from (eqn (1)) as a function of density. The ratio k_n/k_s is shown in the upper panel along with a schematic illustration of k_n and k_s as the inset. (b) Contact radius r_a (black squares) and indentation of a particle δ (blue circles) estimated from the Digby model and experimental δ (red circles) as a function of annealing duration. Inset: Schematic of the NP contact geometry in the Digby model. (c) Bonded radius r_b computed from the Digby, JKR,[42] and DMT[46] models as a function of the annealing duration. All dashed lines are guides for the eye and open symbols refer to the pristine F-0.

computed contact radii. Fig. 5b shows the variation of the contact radius, r_a, estimated from eqn (1a) and (2a) for the silica fibers with the annealing time. For F-0, the value r_a = 12 nm remained virtually unchanged after the initial annealing for 0.5 h and then largely increased to 31 nm as the annealing time was extended to 4 h. According to eqn (1a) and (2a), $r_a \sim k_n/G_{NP} \sim K/K_{NP}$ and hence the similar K/K_{NP} and r_a values for F-0 and F-05 (Fig. 4b) implied that the enhanced K_{NP}, due to a densification of the particles in F-05, could account for the increase in K. For longer annealing, the increase in r_a could be ascribed to the adhesion processes, such as cementation and consolidation. This could be directly evidenced by the decrease in the mutual approach of two NPs' centers, δ, schematically shown in Fig. 5b.

The parameter $\delta = (d - d_c)/2$ helps assess the role of NP adhesion on the increase of r_a in F-2 and F-4. Experimentally, the intercore distance, d_c, (Table 1) and the diameter of the constituent SiO_2 NPs, d, were determined from the SEM images of the silica fibers and NP powders in Fig. S1 (ESI†), respectively. In the Digby model, $\delta = \frac{2r_a(r_a^2 - r_b^2)^{\frac{1}{2}}}{d}$ was related to the contact radius, r_a, and bonded radius, r_b, which were computed from eqn (2). Fig. 5b depicts the experimental and computed δ for the silica fibers. While the approximately similar δ in the pristine F-0 and F-05 excluded cementation, the augmented δ for F-2 was an indication of a cementation effect with prolonged annealing. The computed (blue symbols) δ values capture the experimental (red circles) values for the silica fibers in Fig. 5b (upper panel) except for F-4.

A subtle cementation increase could play a significant role in the growth of the contact grain radius, $r_{a,ce}$, according to the equation, $\frac{2r_{a,ce}}{d} = \left[\left(\frac{2r_{a0}}{d}\right)^2 + \left(\frac{16\Delta p}{3Z}\right)^{1/2}\right]^{1/2}$ proposed by Dvokin *et al.*,[35–38] where the porosity decrease Δp is a consequence of the cementation and r_{a0} is the initial contact radius (Δp = 0). This relation allows weighting the cementation effect on r_a in F-2 and F-4 *via* the comparison between r_a and $r_{a,ce}$. Assuming a decrease Δp = 0.03(0.05) for F-2(F-4) relative to F-05 with r_{a0} = 12 nm, the computed $r_{a,ce}$ = 21.6 nm is comparable to r_a (= 20.3 nm) in F-2, indicating the domination of cementation. For F-4, however, there is a discrepancy between $r_{a,ce}$ = 23 nm, and r_a (= 31 nm) along with an overestimated δ by the Digby model. In light of the covalent bonds between SiO_2 NPs at high temperature,[39] the strong adhesive force of chemical bonding may be responsible for the high r_a in F-4.

In the Digby model, the strong interparticle adhesion is expressed in terms of the bonded area with radius r_b (eqn (2b)), which monotonically increased with the annealing time, as shown in Fig. 5c. The adhesion energy W, defining the work of detaching two interfaces, can be estimated from the fiber's Young's modulus, E, according to Kendall's relation:[40–42]

$$E = A\left(1 - \nu_{NP}^2\right)^{-\frac{2}{3}}(1 - p)^4\left(\frac{WE_{NP}^2}{d}\right)^{\frac{1}{3}} \quad (3)$$

where the dimensionless A (= 16 used in this work) is, in principle, an adjustable parameter. Note that E (eqn (3)) depends on the particle size d. The computed W listed in Table 1 consistently increased with annealing time, and was in the order of the fracture energy of silica in F-2 and F-4 (1–3 J m^{-2})[43] suggesting the formation of covalent siloxane bonds between the NPs.[28] Indeed, the surface OH groups of silica NPs usually undergo the condensation reaction and transform into siloxane bonds at high temperatures.[44] The consumed OH groups can lead to a decrease in the special heat capacity,[45] which was consistently observed in F-2 and F-4 (inset to Fig. 5), implying the presence of condensation reactions. Compared to the specific heat capacity, which depends on the density of OH groups, the sound velocities obtained from BLS allowed sensing the interparticle adhesion force. The latter can be strengthened due to the condensation reaction on OH groups.

The adhesion energy W relates to the bonded radius r_b, which has been taken into account in contact models such as

the Derjaguin–Muller–Toporov (DMT)[46] and Johnson–Kendall–Roberts (JKR) models:[40] $r_{b,DMT} = \left(\frac{\pi d^2 W}{8E_{eff}}\right)^{\frac{1}{3}}$ and $r_{b,JKR} = \left(\frac{3\pi d^2 W}{8E_{eff}}\right)^{\frac{1}{3}}$ where $E_{eff} = \frac{2E_{NP}}{3(1-\nu_{NP})^2}$ for identical contacted particles. The JKR model was proposed for soft and compliant particles with strong adhesion *versus* the DMT model, which is suggested for rigid systems with low adhesion: $r_{b,JKR} > r_{b,DMT}$ for the same contacts. The bonded r_b values from the DMT and JKR models for the four silica fibers are shown in Fig. 5c along with the r_b values from Digby's model. For pristine F-0, r_b = 2.4 nm is similar to $r_{b,DMT}$ (= 2.8 nm), whereas for F-05, r_b = 4.2 nm conformed to $r_{b,JKR}$ (= 4.1 nm). This crossover of r_b from hard DMT to soft JKR contacts could result from the softening of the annealed SiO_2 NPs (at high temperature). For F-2, $r_b \approx r_{b,JKR}$ (= 6 nm) increased well above the value for F-05, mainly because of the newly formed covalent bonds between the NPs, which increased W (Table 1). The chemical nature of the binding molecules on connected nanoparticles plays a crucial role in the elasticities of colloidal films.[7] As compared to the physical bonding (*i.e.*, van der Waals forces), the much stronger chemical bonds (*e.g.*, covalent and hydrogen bonding) have a greater impact with their increasing fraction with annealing time on the fiber elasticity (F-4). For F-4 with the largest adhesion energy W among the four silica fibers, a discrepancy between r_b (= 6.6 nm) and $r_{b,JKR}$ (= 8.6 nm) was observed. We recall the overestimated particle normal displacement, δ, and the contact radius, r_a, for the same sample F-4 (Fig. 5b), which revealed the failure of Digby's model to represent systems with a relatively large adhesion (*e.g.*, F-4). In fact, r_a includes the contribution from r_b at a high W since K ($\sim k_n \sim r_a$), the elastic response of a material to uniform compression, is no longer insensitive to the stiffening caused by adhesion forces over a large area with radius r_b.[47]

Summing up this section, an enhanced elasticity in the annealed fibers is favored by different processes, which include densification, cementation, and the formation of covalent bonds, and their relative contribution depends on the annealing time. The rapid densification process is responsible for the elastic enhancements in a short annealing time (F-05). On the other hand, the cementation and condensation reaction (covalent bonds) processes occur after long-time annealing, and these determined the elastic enhancement in F-2 and F-4. The cementation controlled the K in F-2, and K was further enhanced by the formation of covalent bonds in the case of F-4. A large elasticity usually accompanies a high thermal conductivity κ, which is important for materials applications.[48] To gain insights into the thermal-elastic properties of fibers with distinct interfacial adhesion, we next examine κ at different annealing times.

Thermal conductivity

The thermal conductivity κ (red circles) of the silica fibers measured by the T-bridge method[49–51] is shown in Fig. 6a as a function of the fiber density. The pristine F-0 (open red circle) had $\kappa = 0.14 \pm 0.06$ W m^{-1} K^{-1}, which is about one magnitude lower than the bulk value (= 1.4 W m^{-1} K^{-1}) of fused silica. As the fiber density increased (porosity decreased) with annealing time, κ significantly increased and reached 1.24 ± 0.23 W m^{-1} K^{-1} in F-4. Effective medium models that are usually applied to represent the thermal conductivity of porous materials are based on approximations of coherent potential (CP) and porosity weight medium (PWDM),[52–54] which take into account the effect of a pore's shape and/or size (Section 2.2 in ESI†). It should be noted that these effective medium models for thermal conductivity are typically empirical and quasi-physical. Based on the inset in Fig. 5a, both models could not represent the strong increase of κ with decreasing porosity. Notably, all these effective medium models ignored the interfacial thermal resistance, which is related to the fraction of the interparticle conduction path C_s.[55] As the interfacial contacts were found to greatly impact the speed of sound in all four fibers (Section 2.3), the contribution of C_s to κ should be considered. For particles in contact, $C_s = 2r_a/d$ and the

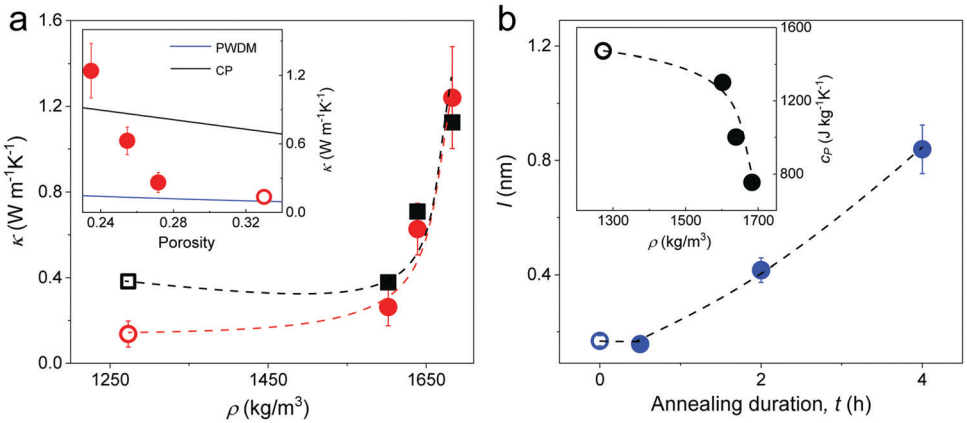

Fig. 6 (a) Experimental (red circles) thermal conductivity κ, and computed $\kappa = C_s\kappa_{NP}$ (black squares) of silica fibers as a function of density. Inset: κ *vs.* porosity along with two effective medium approximations, CP and PWDM (Section 2.2 in ESI†). (b) The computed mean free path l in the fibers at different annealing time. Inset: Specific heat capacity obtained from DSC as a function of fiber density. All the dashed lines are guided to the eye and all open symbols refer to pristine F-0.

computed $\kappa = C_s\kappa_{NP}$[55] (black square) assuming a bulk κ_{NP} = 1.4 W m^{-1} K^{-1} for the SiO_2 NPs, as shown in Fig. 6a. A good agreement between the computed and experimental κ values was observed for the three annealed fibers, corroborating the notion of a contact-induced enhancement of heat transport. For F-0, the interfacial contacts led to an overestimation of the κ probably due to the overestimated (by 120%) κ_{NP} (= κ_{bulk}) due to its more porous SiO_2 NPs. In fact, for the pristine F-0, the SiO_2 NPs were observed to be much softer as compared to the bulk silica (Fig. 3b). Note that the thermal conductivity depended on r_a/d ($\sim C_s$) and thereby its size dependence resembled that of the elastic modulus, E (eqn (3)).

According to the kinetic theory, thermal conductivity is related to the elasticity by $= \frac{1}{3}c_p v l$, where c_p is the specific heat capacity, $v = (c_L + 2c_T)/3$ and is the average sound velocity, and l is the mean free path, respectively. The experimental c_p, determined from differential scanning calorimetry (DSC) is shown in the inset of Fig. 6b, whereas the computed l values in the four fibers are shown in Fig. 6b. The somewhat counter-intuitive decrease in c_p in the three annealed fibers was attributed to the reduction of the surface dangling hydroxyl groups (OH) of the SiO_2 NPs.[56] The latter were transformed into covalent siloxane bonds due to the condensation reactions at high temperatures. Since the c_p = 733 J kg^{-1} K^{-1} of F-4 reached the bulk value of silica (= 754 J kg^{-1} K^{-1}), the OH groups should be completely consumed after 4 h annealing. The computed l qualitatively resembled the dependence of r_a on the annealing time (Fig. 5b). For F-0 and F-05, l = 0.2 nm seemed to be insensitive to the densification of both the SiO_2 NPs and fibers (Table 1). With enlarged contact grains and an enhanced adhesive force, the computed l was significantly increased to 0.4 nm (0.85 nm) for F-2 (F-4). Notably, for F-4, the phonon mean free path became very similar to the value l (= 0.8 nm) for bulk silica.[57] Therefore, the interfacial properties dominated the thermal conductivity of the fibers κ prepared with a long annealing time (F-2 and F-4), while the bulk κ_{NP} of the SiO_2 nanoparticles controlled the κ for the short annealing time (F-05).

Conclusions

We utilized Brillouin light spectroscopy to obtain the full isotropic elasticities of disordered granular silica fibers fabricated *via* crack engineering, and the *in situ* the shear modulus of the constituent nanoparticles at different thermal annealing circles. The BLS study was complemented by thermal conductivity measurements of the same fibers. Our data analysis allowed identifying the contributions of the adhesion processes to both the elastic stiffness and thermal conductivity of silica fibers. Under the framework of the Digby, cemented, and DMT/JKR theoretical models, the contact radius was revealed to control the elastic enhancement. However, the underlined mechanisms affecting the size and impact of the contact radius depended on the annealing time. With a short annealing time (0.5 h), the contacts between the particles barely changed compared to the pristine fiber and the properties of the fibers relied on their constituent NPs. Tiny cementation occurred after prolonged annealing (2 h), leading to a significant increase in the contacts and a pronounced enhancement of the elasticity. However, at a relatively long annealing time (4 h), the cementation effect alone could not account for the sustained strong elasticity enhancement. Instead the adhesive force between the nanoparticles was strengthened by additional contributions from the emerging covalent bonds due to condensation reactions. Surface contact effects were manifested in the thermal conductivity of the same fibers through the interface thermal resistance. The relation between the contacts and heat transport was collaborated by the computed phonon mean free path, which exhibited a large increase as the number of contacts grew.

Conflicts of interest

There are no conflicts to declare.

Acknowledgements

B. L. thanks the financial support from the program of China Scholarships Council (No. 201906260224). G. F. acknowledge the financial support by ERC AdG SmartPhon (Grant No. 694977) and the support by the High-Level Foreign Expert Program of Tongji University. Y. C. acknowledge the financial support by Shanghai Pujiang Program (Grant No. 20PJ1413800). Open Access funding provided by the Max Planck Society.

Notes and references

1 M. A. Kastner, *Phys. Today*, 1993, **46**, 24.
2 Y. Liu, B. Fan, Q. Shi, D. Dong, S. Gong, B. Zhu, R. Fu, S. H. Thang and W. Cheng, *ACS Nano*, 2019, **13**, 6760–6769.
3 K. E. Mueggenburg, X.-M. Lin, R. H. Goldsmith and H. M. Jaeger, *Nat. Mater.*, 2007, **6**, 656–660.
4 Q. Shi and W. Cheng, *Adv. Funct. Mater.*, 2020, **30**, 1902301.
5 C. L. Poyser, T. Czerniuk, A. Akimov, B. T. Diroll, E. A. Gaulding, A. S. Salasyuk, A. J. Kent, D. R. Yakovlev, M. Bayer and C. B. Murray, *ACS Nano*, 2016, **10**, 1163–1169.
6 D. V. Talapin, J.-S. Lee, M. V. Kovalenko and E. V. Shevchenko, *Chem. Rev.*, 2010, **110**, 389–458.
7 A. Ayouch, X. Dieudonné, G. Vaudel, H. Piombini, K. Vallé, V. Gusev, P. Belleville and P. Ruello, *ACS Nano*, 2012, **6**, 10614–10621.
8 E. Alonso-Redondo, M. Schmitt, Z. Urbach, C. Hui, R. Sainidou, P. Rembert, K. Matyjaszewski, M. Bockstaller and G. Fytas, *Nat. Commun.*, 2015, **6**(1), 8309.
9 E. Alonso-Redondo, L. Belliard, K. Rolle, B. Graczykowski, W. Tremel, B. Djafari-Rouhani and G. Fytas, *Sci. Rep.*, 2018, **8**, 16986.
10 B. Graczykowski, N. Vogel, K. Bley, H.-J. R. Butt and G. Fytas, *Nano Lett.*, 2020, **20**, 1883–1889.
11 W. Cheng, J. Wang, U. Jonas, G. Fytas and N. Stefanou, *Nat. Mater.*, 2006, **5**, 830–836.

12 M. Mattarelli, M. Montagna, T. Still, D. Schneider and G. Fytas, *Soft Matter*, 2012, **8**, 4235–4243.
13 H. Kim, Y. Cang, E. Kang, B. Graczykowski, M. Secchi, M. Montagna, R. D. Priestley, E. M. Furst and G. Fytas, *Nat. Commun.*, 2018, **9**, 2918.
14 B. Li, B. Jiang, W. Han, M. He, X. Li, W. Wang, S. W. Hong, M. Byun, S. Lin and Z. Lin, *Angew. Chem., Int. Ed.*, 2017, **56**, 4554–4559.
15 O. Dalstein, E. Gkaniatsou, C. Sicard, O. Sel, H. Perrot, C. Serre, C. Boissière and M. Faustini, *Angew. Chem., Int. Ed.*, 2017, **129**, 14199–14203.
16 J. Xie, J. Guo, D. Wang, Y. Cang, W. Zhang, J. Zhou, B. Peng, Y. Li, J. Cui, L. Chen, G. Fytas and X. Deng, *Adv. Mater. Interfaces*, 2020, 2000222.
17 L. Saviot, S. Le Gallet, F. Demoisson, L. David, G. Sudre, A. Girard, J. Margueritat and A. Mermet, *J. Phys. Chem. C*, 2017, **121**, 2487–2494.
18 A. Girard, J. Ramade, J. Margueritat, D. Machon, L. Saviot, F. Demoisson and A. Mermet, *Nanoscale*, 2018, **10**, 2154–2161.
19 T. Still, M. Mattarelli, D. Kiefer, G. Fytas and M. Montagna, *J. Phys. Chem. Lett.*, 2010, **1**, 2440–2444.
20 W. Cheng, J. Wang, U. Jonas, W. Steffen, G. Fytas, R. Penciu and E. Economou, *J. Chem. Phys.*, 2005, **123**, 121104.
21 E. Kang, H. Kim, L. A. Gray, D. Christie, U. Jonas, B. Graczykowski, E. M. Furst, R. D. Priestley and G. Fytas, *Macromolecules*, 2018, **51**, 8522–8529.
22 H. Lamb, *Proc. R. Soc. London, Ser. A*, 1917, **93**, 114–128.
23 H. Lim, M. Kuok, S. Ng and Z. Wang, *Appl. Phys. Lett.*, 2004, **84**, 4182–4184.
24 N. C. Bell, C. Minelli, J. Tompkins, M. M. Stevens and A. G. Shard, *Langmuir*, 2012, **28**, 10860–10872.
25 D. B. Fraser, *J. Appl. Phys.*, 1968, **39**, 5868–5878.
26 T. Mori and K. Tanaka, *Acta Metall.*, 1973, **21**, 571–574.
27 R. Hill, *J. Mech. Phys. Solids*, 1965, **13**, 213–222.
28 A. Lesaine, D. Bonamy, G. Gauthier, C. L. Rountree and V. Lazarus, *Soft Matter*, 2018, **14**, 3987–3997.
29 P. Digby, *J. Appl. Mech.*, 1981, **48**, 803–808.
30 K. W. Winkler, *Geophys. Res. Lett.*, 1983, **10**, 1073–1076.
31 R. M. German, *Powder Technol.*, 2014, **253**, 368–376.
32 K. L. Johnson and K. L. Johnson, *Contact Mechanics*, Cambridge university press, 1987.
33 A. Norris and D. Johnson, *J. Appl. Mech.*, 1997, **64**, 39–49.
34 V. Langlois and X. Jia, *Powder Technol.*, 2011, **208**, 509–514.
35 J. Dvorkin, A. Nur and H. Yin, *Mech. Mater.*, 1994, **18**, 351–366.
36 J. Dvorkin, *Mech. Mater.*, 1996, **23**, 29–44.
37 J. Dvorkin and D. Yale, *Comput. Geotechn.*, 1997, **20**, 287–302.
38 V. Langlois and X. Jia, *Phys. Rev. E: Stat., Nonlinear, Soft Matter Phys.*, 2014, **89**, 023206.
39 L. Zhang, M. D'Acunzi, M. Kappl, A. Imhof, A. van Blaaderen, H.-J. Butt, R. Graf and D. Vollmer, *Phys. Chem. Chem. Phys.*, 2010, **12**, 15392–15398.
40 K. L. Johnson, K. Kendall and A. Roberts, *Proc. R. Soc. London, Ser. A*, 1971, **324**, 301–313.
41 K. Kendall, N. M. Alford and J. D. Birchall, *Proc. R. Soc. London, Ser. A*, 1987, **412**, 269–283.
42 K. Kendall, *Molecular Adhesion and Its Applications: The Sticky Universe*, Springer Science & Business Media, 2007.
43 T. Rouxel, *J. Am. Ceram. Soc.*, 2007, **90**, 3019–3039.
44 C. J. Brinker and G. W. Scherer, *Sol–Gel Science: The Physics and Chemistry of Sol–Gel Processing*, Academic press, 2013.
45 L. Zhuravlev, *Langmuir*, 1987, **3**, 316–318.
46 B. V. Derjaguin, V. M. Muller and Y. P. Toporov, *J. Colloid Interface Sci.*, 1975, **53**, 314–326.
47 Y. Cang, Z. Wang, C. Bishop, L. Yu, M. Ediger and G. Fytas, *Adv. Funct. Mater.*, 2020, **30**, 2001481.
48 Z. Wang, K. Rolle, T. Schilling, P. Hummel, A. Philipp, B. A. Kopera, A. M. Lechner, M. Retsch, J. Breu and G. Fytas, *Angew. Chem., Int. Ed.*, 2020, **132**, 1302–1310.
49 M. Fujii, X. Zhang, H. Xie, H. Ago, K. Takahashi, T. Ikuta, H. Abe and T. Shimizu, *Phys. Rev. Lett.*, 2005, **95**, 065502.
50 W. Jang, W. Bao, L. Jing, C. Lau and C. Dames, *Appl. Phys. Lett.*, 2013, **103**, 133102.
51 J. Kim, D.-J. Seo, H. Park, H. Kim, H.-J. Choi and W. Kim, *Rev. Sci. Instrum.*, 2017, **88**, 054902.
52 B.-Y. Tsui, C.-C. Yang and K.-L. Fang, *IEEE Trans. Electron Devices*, 2004, **51**, 20–27.
53 T. Coquil, E. K. Richman, N. J. Hutchinson, S. H. Tolbert and L. Pilon, *J. Appl. Phys.*, 2009, **106**, 034910.
54 W. Zhu, G. Zheng, S. Cao and H. He, *Sci. Rep.*, 2018, **8**, 10537.
55 M. Liu, L. Qiu, X. Zheng, J. Zhu and D. Tang, *J. Appl. Phys.*, 2014, **116**, 093503.
56 M. Marszewski, D. Butts, E. Lan, Y. Yan, S. C. King, P. E. McNeil, T. Galy, B. Dunn, S. H. Tolbert and Y. Hu, *Appl. Phys. Lett.*, 2018, **112**, 201903.
57 C. Kittel, *Phys. Rev.*, 1949, **75**, 972.